

TUNL REU VI

RESEARCH REPORT

18 MAY 2020 – 25 JULY 2020



TRIANGLE UNIVERSITIES NUCLEAR LABORATORY

Duke University  
North Carolina Central University  
North Carolina State University  
University of North Carolina at Chapel Hill

Box 90308, Durham, North Carolina 27708-0308, USA

The research described in this report is supported by the United States Department of Energy, Office of Science, under:

Grant No. DE-SC0010007 (Duke University High-Energy Physics Group),  
Grant No. DE-FG02-97ER41033 (Duke University/TUNL),  
Grant No. DE-FG02-97ER41042 (North Carolina State University), and  
Grant No. DE-FG02-97ER41041 (University of North Carolina).

The TUNL Research Experiences for Undergraduates (REU) Program is supported by the National Science Foundation under:

Grant No. NSF-PHY-1757783.

# Contents

<b>Introduction</b>	<b>iv</b>
<b>Personnel</b>	<b>v</b>
<b>1 Research Based at Duke</b>	<b>1</b>
1.1 Di-Hadron Analysis for the Electron Ion Collider . . . . .	2
1.2 Calculation of Neutrino Events in Binary Neutron Star Mergers . . . . .	4
1.3 Reconstructing Cross Sections in the Enge Focal Plane . . . . .	7
1.4 Determining Critical Reactions in Low-Mass X-ray Binaries . . . . .	10
1.5 Data Evaluation of ${}^9\text{C}$ . . . . .	13
1.6 Analysis of Activation Data for Short-Lived Radioisotopes using the RABITTS Transfer System	15
<b>2 Research Based at CERN</b>	<b>17</b>
2.1 Exploring Track Trigger Parameters for SUEPs . . . . .	18
2.2 Using Machine Learning to Improve the Sensitivity of $t\bar{t}$ Resonance Searches . . . . .	21

# Introduction

An important national goal is to develop a diverse, internationally competitive, and globally engaged workforce in science and engineering. The Research Experiences for Undergraduates (REU) program is part of the effort to achieve that goal. The REU program at the Triangle Universities Nuclear Laboratory (TUNL) and Duke University provides a ten-week opportunity for undergraduate students to pursue research in the areas of nuclear and particle physics. This allows promising physics majors to broaden their education through participation in research at the frontiers of these exciting scientific fields.

In 2020, due to the COVID-19 pandemic the program was provided in a virtual format. Nine students participated in the TUNL REU Program: six worked with faculty from the TUNL consortium institutions on nuclear physics projects, while three students worked with faculty from the Duke High-Energy Physics (HEP) group on particle physics projects related to research at CERN. As is the case for an in-person experience, having the nuclear and particle physics students in the same program facilitated cross-field intellectual exchange and the sharing of resources needed by both groups, while the participation of the HEP group in the program gives it an international component.

Through introductory lectures and direct research involvement, the students gain experience and insights in the main stages of scientific research in nuclear and particle physics:

- The development of concepts to probe specific features of nuclear matter, particles and fields;
- The design, construction, testing, and installation of equipment and instrumentation;
- Data acquisition, analysis, and interpretation; and
- The dissemination of research results.

In addition to direct involvement in research projects, the REU program at Duke includes activities that are designed to broaden the students' physics foundation, enhance their research skills, and build confidence. These activities include: (1) regular meetings with the program coordinator, (2) research tutorials and special topic lectures, (3) a science writing tutorial, and (4) a required report and presentation by each student at the end of the program. The research reports written by the students form the main body of this document.

# Personnel

## 2020 TUNL REU Participants

<i>Student</i>	<i>Home Institution</i>	<i>Faculty Advisor(s)</i>	<i>Class</i>
Olivia Dickinson	Providence College	Krishichayan	Jr
Briana Evans	University of Texas at Dallas	James Beacham	Jr
Beshoi Grees	Lipscomb University	John Kelley	Jr
Ian Lapinski	Shippensburg University	Amber Lauer	Jr
Jessica Nelson	Westminster College	Kate Paschal	Jr
Angelina Partenheimer	Truman State University	Mark Kruse	Jr
Loida Rosado	University of Puerto Rico	Kate Scholberg	So
Briana Strickland	Ursinus College	Richard Longland	Jr
Megan Sturm	University of Connecticut	Anselm Vossen	Jr

## 2020 TUNL REU Administration

*Principal Investigator and Program Director:*  
Dr. Alexander Crowell

*Co-Principal Investigator and CERN Experience Director:*  
Professor Ayana Arce



PARTICIPANTS IN THE 2020 TUNL RESEARCH EXPERIENCES FOR UNDERGRADUATES (REU) PROGRAM. SHOWN IN THE PHOTOGRAPHS FROM LEFT TO RIGHT ARE: (TOP ROW) ANGELINA PARTENHEIMER (TRUMAN STATE UNIVERSITY), IAN LAPINSKI (SHIPPENSBURG UNIVERSITY), BRIANA EVANS (UNIVERSITY OF TEXAS AT DALLAS); (MIDDLE ROW) BESHOI GREES (LIPSCOMB UNIVERSITY), JESSICA NELSON (WESTMINSTER COLLEGE), MEGAN STURM (UNIVERSITY OF CONNECTICUT)); (BOTTOM ROW) BRIANA STRICKLAND (URSINUS COLLEGE), OLIVIA DICKINSON (PROVIDENCE COLLEGE), LOIDA ROSADO (UNIVERSITY OF PUERTO RICO).

# Research Based at Duke

---

Chapter 1

## 1.1 Di-Hadron Analysis for the Electron Ion Collider

M. STURM, *University of Connecticut, Storrs, CT*; A. VOSSEN, *Duke University, Durham, NC*

Scattering accelerated electrons off protons and detecting the final state particles of the collisions allow us to study the internal structure of nucleons. The Electron Ion Collider (EIC) is being designed for construction at Brookhaven National Laboratory (BNL) and a report is currently being developed to outline the detector and collider parameters based on the requirements of the various physics channels. This project will contribute to the report by developing software to simulate specific aspects of di-hadron production in semi-inclusive deep inelastic scattering (SIDIS). In particular, we studied detector resolutions based on the true and detector smeared kinematics and implemented a weighting scheme to simulate polarization effects in the cross section based on theoretical models. In addition to charged neutral pions, we also studied neutral pions which were reconstructed from photon pairs. With these improvements, more accurate and comprehensive simulations can be used in the report.

The EIC will be built off of RHIC (the Relativistic Heavy Ion Collider), the current accelerator at BNL. It will maintain the infrastructure to accelerate protons and add a second acceleration ring to produce an electron beam. When protons collide with electrons, a virtual photon is exchanged. At high energies, this photon is exchanged with a constituent quark, allowing for observation of fundamental particles in the internal structure of the proton and providing further insight on the strong nuclear force. Additionally, with polarized proton and electron beams, the EIC will be able to make measurements on the contributors to proton spin, including quarks and gluons [Ans20].

Currently the EIC User Group is creating a yellow report to serve as a detailed plan for the development of the EIC. This report will be comprised of thorough studies on current and possible new physics topics and how to effectively design detectors and experiments to measure them. Our work this summer will contribute to the yellow report.

Our research group is part of the SIDIS working group. SIDIS is a type of scattering between a lepton and nucleus, mediated by a virtual photon, where the outgoing lepton ( $l'$ ) and hadron(s) ( $P_{h1}$  and  $P_{h2}$ ) are observed. This process is depicted in Figure 1.1.

The observation of both the lepton and hadron(s) allows for event information to be deduced based on the calculated kinematics of the detected particles. The cross section of this type of scattering event can be broken down into contributions from parton distribution functions, perturbative QCD and fragmentation functions ( $\sigma \propto f * \hat{\sigma} * FF$ ).

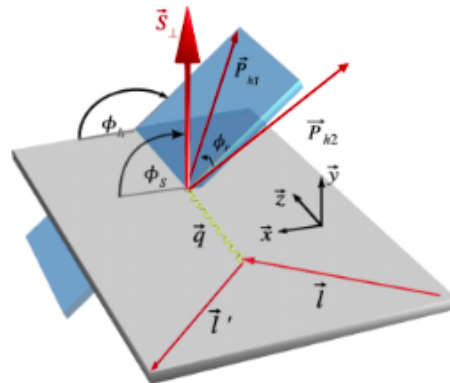


Figure 1.1: Illustration of the kinematic variables in a di-hadron SIDIS process.

Parton distribution functions are probabilistic descriptions of how the constituents of particles are distributed [Met16]. Fragmentation functions describe how the cross section is impacted based on the relative polarization of the nucleus and its constituent quarks. Furthermore, their angular dependences access different quark quantum numbers, meaning that information about the original nucleus can be inferred from the observed asymmetries in the detected angles of the outgoing hadron ( $\phi_h$ ) and lepton ( $\phi_s$ ).

Our work specifically focused on di-hadron observation, for which the relative momenta of the outgoing hadrons provide an extra degree of freedom in the asymmetry measurements. Therefore in addition to  $\phi_h$  and  $\phi_s$  we also measure  $\phi_R$  between the hadrons.

A C++ plugin was already written for analysis of di-hadron events for Monte-Carlo generated and smeared events by Christopher Dilks and is available on gitlab [Dil20]. The plugin paired hadrons and electrons from the same scattering event and performed relevant kinematic calculations. The goal of this project was to further develop the plugin.

We first implemented a connection between corresponding smeared and generated events. While generated data contains all particle and event information exactly as it was created, smeared data simulates how a detector would measure those events.

In order to make a connection between the two, we labeled events based on the id of the particle in the original generated particle list. Once the connection was made, we could examine the resolution, given by the equation  $Resolution = \frac{Smeared - Unsmearred}{Unsmearred}$

With this equation we could first test that our connection was correct, by checking the resolution of unsmearred characteristics such as particle PDG, which identifies the type of particle. We observed this resolution to have a mean and standard deviation of zero, meaning that the connection was successful. On the other hand, for smeared characteristics, such as energy, we observe a distribution. These variations in observed quantities propagate through the kinematic calculations, resulting in a distribution for the resolution of kinematic variables such as  $Q^2$ .

Certain short-lived particles do not appear in smeared data and instead require reconstruction. We reconstructed  $\pi^0$ s using the energy and angles of resulting photons. Initially, we identified all smeared photon pair combinations and by plotting their reconstructed invariant mass observed a peak at the  $\pi^0$  mass and another smaller peak at the  $\eta$  mass (see Figure 1.2).

After implementing cuts on the reconstructed mass ( $.12 \text{ GeV} < M < .15 \text{ GeV}$ ) and the energy of the photons ( $E > .1 \text{ GeV}$ ) we honed in on the photon pairs that most likely came from a  $\pi^0$ . In comparing this reconstructed mass with the generated mass of the real  $\pi^0$ s we see that the mean is about the same, however the standard deviation is much greater for the reconstructed data, due to the smearing and the reconstruction process.

Once these particles were identified as  $\pi^0$ s they are inserted to the particle list and can be used in the subsequent di-hadron pairing. Currently there is no generated-smeared connection for these reconstructed  $\pi^0$ s, however, once ancestry information becomes available in the software the connection can be made using checks on the generated

$\pi^0$  daughter photon and smeared photon ids.

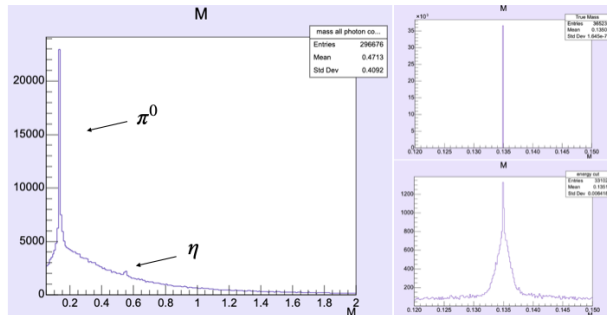


**Figure 1.2: Reconstructed mass of all smeared photon pairs (left). Generated (top right) and reconstructed (bottom right)  $\pi^0$  mass with cuts on energy and mass.**

Our current channel, ( $\pi^+/\pi^-$ ) is equally likely to come from up or down quark. With  $\pi^0$  reconstruction, however, projections can be made for the  $\pi^+/\pi^0$  channel given the assumed data collected by the EIC. This will be more sensitive to the different quark flavors (i.e.  $\pi^+/\pi^0$  will more likely come from up, whereas  $\pi^-/\pi^0$  from down).

Weighting is used to account for theoretical probabilities of certain events occurring. To apply the correct weight, we use transversity grids consisting of different cross section values calculated from variations in observables  $Q^2, z, x$  and  $M$ . The transversity grids provide an amplitude, so the correct weight can be calculated using the formula  $1 + polarization * amplitude * \sin(\phi_s + \phi_r)$ .

The appropriate cross section can be identified in the transversity grid based on generated values of the observables. Then, with the generated-smeared connection, the weight can be applied to the corresponding smeared event.

This weighted cross section can be used to estimate the sensitivity of the proposed EIC for these channels and determine what impact it might have for our understanding of the nucleon structure. Therefore, these studies are an important input to the detector design requirements.

[Ans20] M. Anselmino, A. Mukherjee, and A. Vossen, Prog. Part. Nucl. Phys., **114**, 103806 (2020).

[Dil20] C. Dilks, 2020, <https://gitlab.com/c.dilks/eicsim>.

[Met16] A. Metz and A. Vossen, Prog. Part. Nucl. Phys., **91**, 136 (2016).

---

## 1.2 Calculation of Neutrino Events in Binary Neutron Star Mergers

---

L. ROSADO DEL RIO, *University of Puerto Rico, San Juan, PR*; K. SCHOLBERG, *Duke University, Durham, NC*

**Binary neutron star mergers produce thermal neutrinos that can be observed using detectors such as Super-Kamiokande and the DUNE far detector. Using a software package called SNOwGLoBES we can simulate a neutrino flux from a merger at 10 kpc and calculate its interaction and event distribution rates. We found that for such a merger 4,000 events in DUNE will be detected at 10 kpc, of which 3,500 will be electron neutrino on  $^{40}\text{Ar}$  interactions. We also saw that while the event rates for this merger and for a core-collapse supernova were similar, the neutrino flux for the binary star merger was by one order of magnitude than the flux for the supernova.**

Binary neutron star mergers happen when two neutron stars that are orbiting each other closely spiral inward due to gravitational radiation. The collision of the two forms either a massive neutron star or a black hole, depending on the mass of the stars. The mergers emit gravitational waves that can be used for their detection and observation [Cho17]. Since the mergers heat up high-density material, thermal neutrinos are also emitted from their remnants [Kyu18]. These neutrinos can then be observed by detectors such as Super-Kamiokande and DUNE.

The Deep Underground Neutrino Experiment (DUNE) centers around neutrino science and proton decay studies. It consists of two detectors placed in a neutrino beam, one near the beam source at Fermi National Accelerator Laboratory (near detector), and one at the Sanford Underground Research Laboratory (far detector). The far detector is a 40-kiloton liquid argon detector that uses Liquid Argon Time-Projection Chamber technology for particle identification and background rejection [Dun20]. For this project we will be calculating neutrino events that would be observed using the DUNE far detector.

Neutrinos carry lots of information that can be used to understand the universe and its origins, which is why a software package called SNOwGLoBES [Bec18] is useful for calculating the interaction rates and distributions for supernova burst neutrinos.

Using SNOwGLoBES we can also simulate neutrino fluxes based on a set of parameters that include the average energy and luminosity of the neutrinos and a pinching parameter which controls the high-energy tail of the distribution. For this project,

the goal was to calculate the event distribution for a merger at 10 kpc, which would be just beyond the center of the Milky Way. To that end we established the parameters based on the properties of a merger where the pinching parameter is 2.31 (no pinching), an average energy of 10 MeV, and a luminosity of  $1 \times 10^{53}$  erg/s [Kyu18]. Using these parameters, we can parameterize the spectral shape of the flux using Eqn. 1.1, where  $\alpha$  is the pinching parameter,  $E_v$  is the average energy and  $N$  is related to the luminosity parameter [Sch12]. This project is the first time a signal from a merger has been calculated using a liquid argon detector like the DUNE far detector.

$$\phi(E_v) = N \left( \frac{E_v}{\langle E_v \rangle} \right)^\alpha \exp \left[ -(\alpha + 1) \frac{E_v}{\langle E_v \rangle} \right] \quad (1.1)$$

Table 1.1 shows the distribution of events for each channel interaction, where  $\nu_x$  includes the muon and tau flavors. The total number of events for the merger is 4,733 and the channel with the most interactions is the  $\nu_e$  on argon interaction with 3,559 events.

**Table 1.1: Event Distribution Rates for Merger Flux**

Channel	Events
$\nu_e + e^- \rightarrow \nu_e + e^-$	259.0326
$\bar{\nu}_e + e^- \rightarrow \bar{\nu}_e + e^-$	64.11042
$\nu_x + e^- \rightarrow \nu_x + e^-$	83.5488
$\bar{\nu}_x + e^- \rightarrow \bar{\nu}_x + e^-$	67.73418
$\nu_e + ^{40}\text{Ar} \rightarrow \nu_e + ^{40}\text{K}$	3559.03
$\bar{\nu}_e + ^{40}\text{Ar} \rightarrow \bar{\nu}_e + ^{40}\text{Cl}$	47.6325

We can plot the event distribution to show the expected fluence, referred to as flux, of the emitted neutrinos per 0.2 MeV per  $\text{cm}^2$ . The estimated

neutrino flux for the merger (see Fig. 1.3) shows the distribution of events for different flavors, where the  $\nu_e$  has the same flux as its antiparticle, of approximately  $3.15 \times 10^{11}$ , and the muon and tau flavors are around  $1.4 \times 10^{12}$ . We then can compare this flux to the estimated flux for a core-collapse supernova.

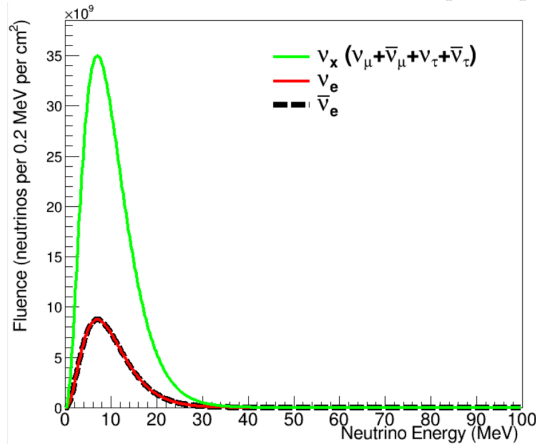


Figure 1.3: Merger flux

In the supernova flux plot (Fig. 1.4) the flux for the electron neutrino is approximately  $3.8 \times 10^{10}$ , while the flux for the muon and tau flavors is about  $2.2 \times 10^{11}$ . We can see that the merger flux is larger by an order of magnitude than the flux that is typically seen for supernova burst neutrinos, even though they have similar event numbers, and that the flux energy for the merger is lower than for the supernova. The smeared rates (Fig. 1.5) show the event rates as a function of detected energy, where the main interaction is the electron neutrino on  $^{40}\text{Ar}$  interaction with around 3,500 events.

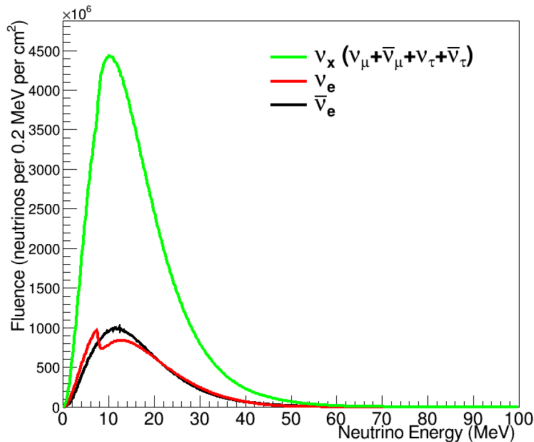


Figure 1.4: Core-collapse Supernova flux

From the resulting figures, we can see that the main interaction is the  $\nu_e$  interaction and that the total number of neutrino events was approximately 4,000, of which around 3,500 were  $\nu_e$  on  $^{40}\text{Ar}$  interactions. Finally, we notice that the neutrino flux for a binary neutron star merger is higher than the flux for a supernova by approximately one order of magnitude. This difference is because, while the event numbers for both are similar, the energy for the merger is lower than that of the supernova. The convolution of flux and cross section gives us the event rate and, since the cross section increases with the energy (Fig. 1.6), high-energy neutrinos lead to a higher event rate. By calculating the events for a binary neutron star merger in a liquid argon detector, we get a first look at what the phenomenon might look like from Earth as we research its properties and effects.

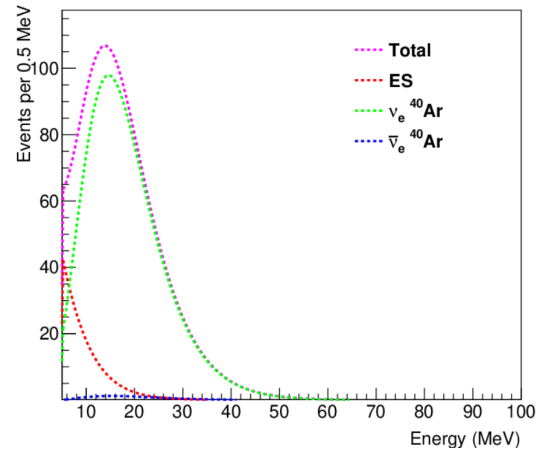


Figure 1.5: Smeared Rates

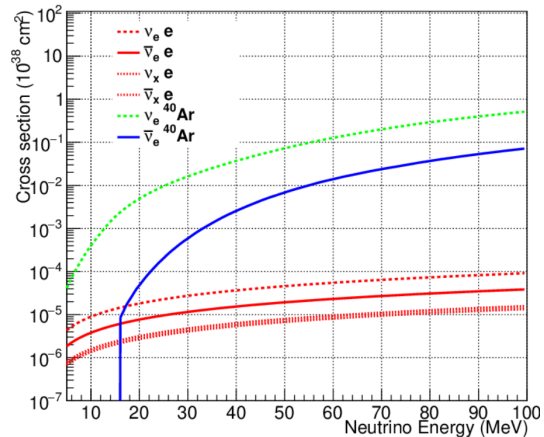


Figure 1.6: Liquid argon cross section

- [Bec18] A. Beck *et al.*, *SNOWGLOBES: SuperNova Observatories with GLOBES*, <https://github.com/SNOWGLOBES/snowglobes>, 2018.
- [Cho17] A. Cho, *Science*, **358**, 282 (2017).
- [Dun20] *Deep Underground Neutrino Experiment*, <https://www.dunescience.org>, 2020.
- [Kyu18] K. Kyutoku and K. Kashiyama, *Phys.Rev. D*, **97** (2018).
- [Sch12] K. Scholberg, *Ann. Rev. Nucl. Part. Sci.*, **62**, 81 (2012).

### 1.3 Reconstructing Cross Sections in the Enge Focal Plane

B. STRICKLAND, *Ursinus College, Collegeville, PA*; R. LONGLAND, *TUNL*

A new method has been developed to reconstruct cross sections through the Focal Plane Detector of the Enge Split-Pole Spectrograph. This method was achieved by sub-dividing the particles going through the detector and measuring their positions in the front of the detector and again in the back of the detector. We have tested this new method with well-known cross sections using GEANT4 software. The results of this reconstruction are finer, more detailed cross-section calculations.

In the Enge Split-Pole Spectrograph, particles exit the target chamber, go through a magnet in which they are bent depending on their incoming momentum, and are then focused into the Focal Plane Detector as shown in Figure 1.7 [Mar19]. In order to take measurements at different values of  $\theta$  (labeled in Fig. 1.7), we have to move the entire spectrograph around the target chamber. Using our old method, we would measure cross sections by moving the spectrograph to some angle  $\theta$ , counting the number of particles entering the detector, then calculating the differential cross section as

$$\frac{d\sigma}{d\Omega} = \frac{\text{number of particles measured at } \theta}{\text{Number of beam particles} * d\Omega}.$$

The issue with this method is that the particles exiting the target chamber actually span some range of  $\theta$  values, but are measured at only one  $\theta$  value. Thus with this method, we are essentially measuring the average cross section for a range of  $\theta$  values.

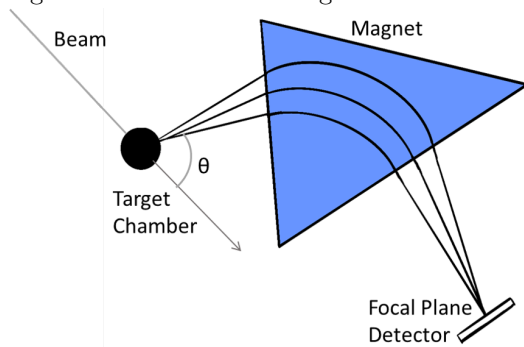


Figure 1.7: A schematic of particles going through the Enge Split-Pole Spectrograph.

Within our Focal Plane Detector, we measure the

position of particles entering the front of the detector and the position of particles in the back of the detector. With these position measurements, we can reconstruct these cross sections by sub-dividing the particles entering the detector. We can achieve this by calculating the angle at which the particle enters the detector, which we will call  $\phi$ , using the measured positions (see Fig. 1.8). Then, we can use these  $\phi$  values to calculate the cross sections and corresponding  $\theta$  values.

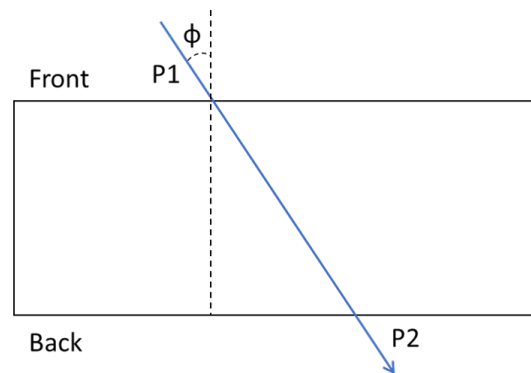
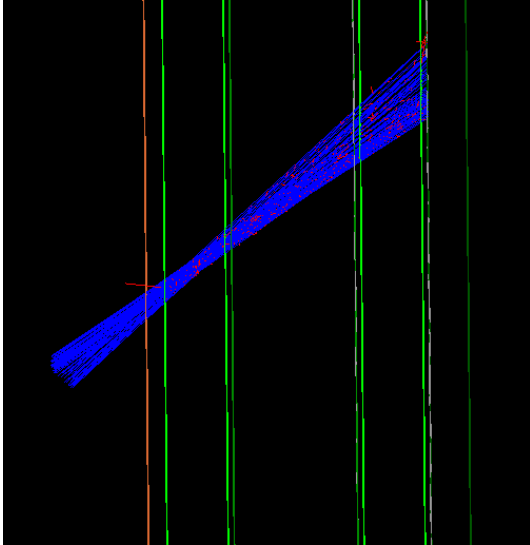


Figure 1.8: Schematic showing a particle entering our detector. The position of this particle would be measured in the front of the detector and again in the back of the detector.

To develop this new method, we need to test it with perfectly known cross sections. We simulate these well-known cross-section environments using GEANT4 software. Our GEANT4 code simulates our detector and particles going through our detector (see Fig. 1.9).



**Figure 1.9:** This is a hollow image of the Focal Plane Detector from our GEANT4 simulations. The blue lines are alpha particles going through the detector. The red lines are scattered electrons.

Since we now want to test this method with well-known cross sections, the easiest test would be to look at an isotropic distribution. In this environment, we would expect to see that all of the angles have the same cross sections, or probabilities. After putting these simulation measurements through our new method, this is exactly the result we saw (left plot on Fig. 1.10). The next simple test we looked at was changing the isotropic source to resemble a linear function. In this setting, the lower angles have a smaller measured cross section than the cross sections of the higher angles (right plot in Fig. 1.10).

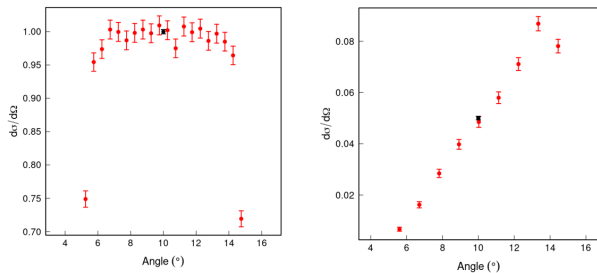


**Figure 1.10:** Left: Plot showing the results of our isotropic source test. Right: Plot showing the results of our linear source test. In both graphs, the black point represents the average cross section for the entire  $10^\circ$   $\theta$  span. The red points represent the measured cross section with the new reconstruction method.

If you look at Figure 1.10, you can see that on the very edges of the  $\theta$  range we have a drop in the cross-section measurements. This is something that was expected, and is caused by increased scattering on the ends of the  $\theta$  range. We can use these simple test environments to help us characterize these dips and show us our limitations with this new method. This analysis is important to look at, because it shows us the limitations of our new reconstruction method. The limitation we are seeing here is even though our range of  $\theta$  values is  $10^\circ$ , we can only successfully reconstruct a range of 8 or  $9^\circ$ . This reconstruction range value varies depending on the particle type and energy.

Our final test of this method was to simulate a realistic cross-section environment. The results of this test are seen in Figure 1.11. The black points in this figure are the measured cross sections using the old method [Set19]. These are the average cross sections for  $\theta$  spans of  $10^\circ$ . The red points represent the measured cross sections for our new sub-dividing method. From this new method, we can see much more detail in our data.

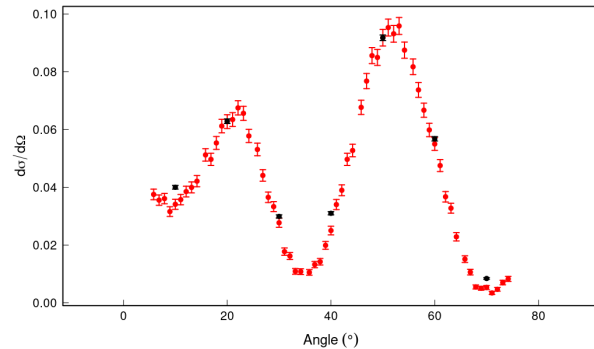


**Figure 1.11:** Results of a realistic cross-section test for our reconstruction method.

We next took the average and sub-divided cross-section measurements and ran both results through model fits. We fit the results using a distorted wave Born approximation elastic scattering model. On the left of Figure 1.12, we have the model fit of the average cross section measurements. The green line is the fit line along with the error band. The orange line is the true parameters that we simulated in GEANT4. These two lines disagree with each other quite a bit. The right side image in Figure 1.12 shows the results of the model fit for our sub-divided cross section measurements. In this fit, you can just barely see the

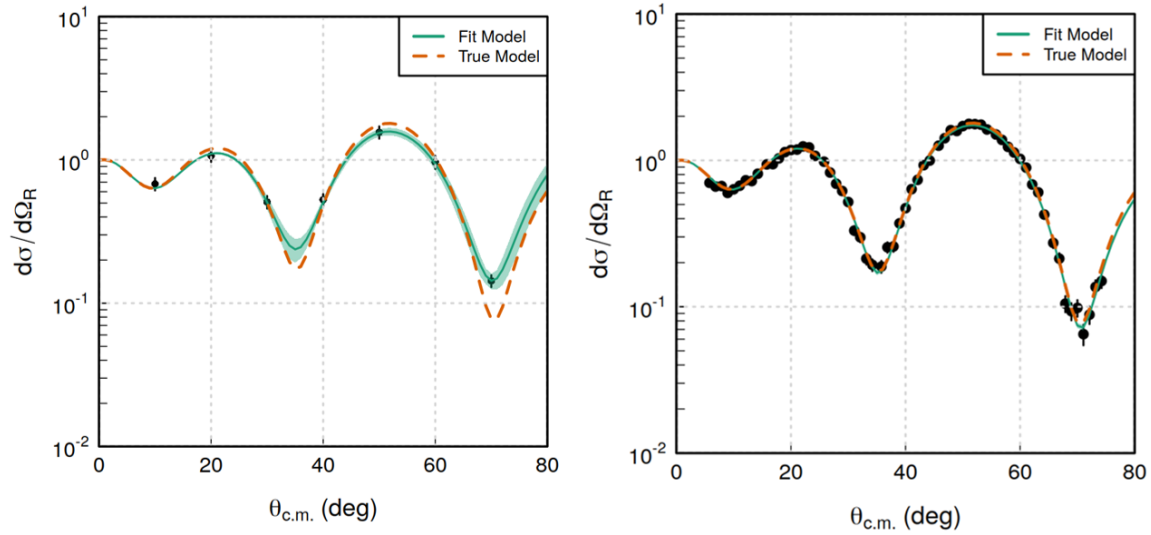


Figure 1.12: These plots show the model fits for both the average cross-section method (left graph) and the sub-divided cross section method (right graph). The cross sections are displayed on a log scale. The choice of a log scale helps to emphasize any discrepancies.

green fit line since it is right on top of the true parameter line. From this comparison, we can see that with this new method we can achieve much finer data. The next step is to test this in the lab.

[Mar19] C. Marshall *et al.*, IEEE Trans. Instrum. Meas., **68**, 533 (2019).

[Set19] K. Setoodehnia *et al.*, Phys. Rev. C, **99**, 055812 (2019).

---

## 1.4 Determining Critical Reactions in Low-Mass X-ray Binaries

---

IAN LAPINSKI, *Shippensburg University, Shippensburg, PA*; AMBER LAUER, *TUNL*

**Stellar models of Low-Mass X-ray Binaries (LMXB's) with co-processed nuclear networks have been created using the Modules for Experiments in Stellar Astrophysics (MESA) to conduct a 2-part sensitivity study on nucleosynthesis. A single reaction rate has been altered for each model to determine the effect the reaction has on observables, elemental abundances, and other metrics. This work will describe analysis designed and completed to identify these reactions. The study is currently ongoing, but most preliminary analysis has been completed.**

Low Mass X-ray Binaries (LMXB's) are characterized by a neutron star accreting matter from a hydrogen and helium-rich companion, causing periodic thermonuclear explosions known as Type-I X-ray bursts (XRB's) [Sch06]. As hydrogen and helium-rich matter from the companion star reaches the neutron star surface, helium is steadily created by the Hot Carbon-Nitrogen-Oxygen (HCNO) cycles, but does not readily fuse and instead sinks deeper into the surface [Ili08]. When this layer, compressed by further accretion, reaches an electron-degenerate state known as a thin-shell instability, the helium is ignited by the triple- $\alpha$  reaction, causing a thermonuclear runaway [Ili08].

The nuclear runaway typically lasts fractions of a second. This is followed by a radiative cooling phase that occurs over the following 10-100s [In'11] and is observed as an X-ray outburst on the order of  $10^{39} - 10^{40}$  ergs [Sch06]. The resulting increase in luminosity make X-ray binaries some of the brightest extra-solar objects [Sch06]. These bursts are the most frequently observed thermonuclear explosions in nature [Cyb16], and serve as a natural laboratory to conduct research on nucleosynthesis in extreme conditions [Sch06]. During the burst, intense heating of the neutron star photosphere produces the majority of the X-ray flux, thus making the resulting spectrum abundant in information about the star's composition [Sch06].

The resulting XRB is extremely complex and depends greatly on reaction rates of certain nuclear processes that are yet to be experimentally determined [Sch06]. This study aims to determine which reactions need to be prioritized for study in the lab to advance understanding of stellar nucleosynthesis, neu-

tron stars, and LMXB's.

Stellar models of an XRB were created using the Modules for Experiments in Stellar Astrophysics (MESA). A neutron star was simulated with an inert core and an active multi-zone outer region with an accretion rate and composition similar to observed values. The models were equipped with a co-processed nuclear network featuring 305 species and over 1600 reactions and their inverses.

The co-processed nuclear network allows for the equations of stellar evolution to be coupled to the network for each time-step of the evolution. A stellar evolution model was created with a singular reaction rate modified for all reactions in the network. A baseline model was created featuring current theoretical reaction rates to determine the effect each reaction has on its observables, final abundances, and other related metrics.

The study is broken into two major sections, which shall be referenced as Part I and Part II. Part I is a coarse resolution study of all reactions in the network. In this first portion, the rate's upper and lower limits are altered by a factor of  $10^2$  and  $10^{-2}$  respectively, far outside the uncertainties. While these new rates may be unrealistically high or low, they allow determining the reactions with the largest effects on the evolution. Part II is planned as a fine-resolution study of  $\sim 200$  reactions which show the largest variation from the baseline. The reaction rates in this portion of the study will be varied within their respective uncertainties using information extracted using ReacSamp, a program created by Carl Fields to sample reaction rates using Monte Carlo methods [Fie16].

In both parts of the study, the models were compared to the baseline using the following metrics: in-

tegrated luminosity, maximum luminosity, integrated energy, maximum energy, burst frequency, and isotopic abundances.

A burst-counting code, written in python, was inherited and expanded to include average burst period calculations by the following equation

$$T = \frac{\sum_{i=1}^{n-1} (t_{i+1} - t_i)}{n} \quad (1.2)$$

Here,  $T$  is the average burst period,  $t_i$  is the time associated with the burst peak, and  $n$  is the total number of bursts. Like many of the metrics in this study, this value was further scaled by comparing the ratio to the baseline to get a more intuitive value.

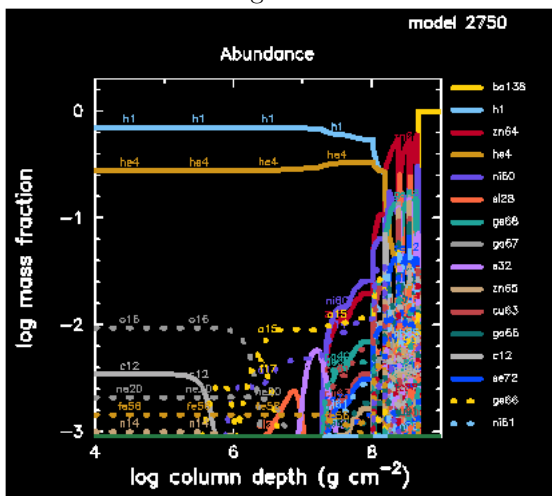


Figure 1.13: Example of an isotopic abundance profile generated with MESA.

In order to compare isotopic mass fractions, the abundance profile of each model must be printed and analyzed at a uniform benchmark point in the star's evolution. To compare models at similar points in their respective evolutions, the selected benchmark is at the end of the radiative cooling phase after the third burst.

This point was located by finding the point where the star's luminosity returns to pre-burst levels. The following calculation was performed to determine the benchmark point:

$$\log(L) < \frac{1}{2} \times \log(L_{peak}) \quad (1.3)$$

where  $L$  is the star's luminosity, and  $L_{peak}$  is the maximum luminosity of the third X-ray burst. This was again scaled relative to the baseline.

The models can be restarted each 500 timesteps, so the closest reset point before the benchmark is also calculated. This allows the abundance profiles to be printed without running the entire evolution, lessening the computational load.

As seen in Fig. 1.13, each abundance profile contains isotopic mass fractions for each zone in the model. The total mass fractions of all isotopes were calculated for the zones in which the optical depth,  $\tau < 1$ . A value of  $\tau > 1$  signifies an opaque zone, so the effect on the spectra is minimal. The following equation was used to compute the mass fractions:

$$X_{tot} = \frac{\sum_i^{\tau < 1} X_i \times dm_i}{M} \quad (1.4)$$

where  $X_{tot}$  is the mass fraction down to the optical depth,  $X_i$  is the mass fraction of zone  $i$ ,  $M$  is the total mass of all zones in which  $\tau < 1$ , and  $dm_i$  is the mass of zone  $i$ . These mass fractions are then compared to the baseline to determine the differences in abundances caused by the modified reaction.

The light curve is a plot of luminosity as a function of time over the duration of the burst with the peak centered at  $t = 0$ , as seen in Fig. 1.14. The light curves used in this study are constructed on the time-scale  $t \in [t_{peak} - 10s, t_{peak} + 150s]$ .

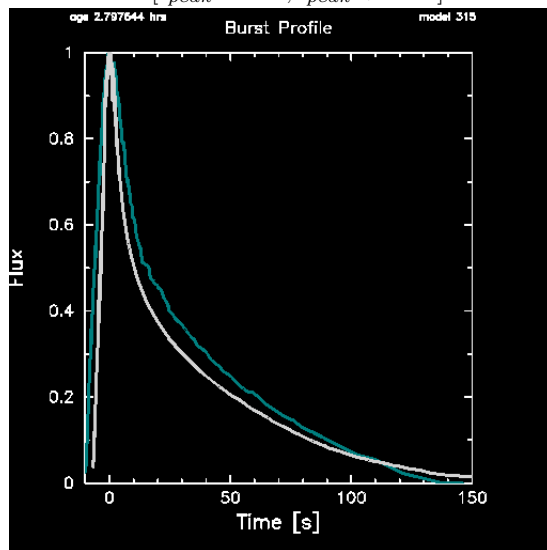


Figure 1.14: Normalized light curve generated with MESA.

A python script was created that scans points around each burst to create lists of luminosity points within the specified domain and records the maximum luminosity of all bursts. These luminosity lists

are then converted to NumPy arrays and interpolated linearly to evaluate the luminosity function on the set

$$t : [-10, -9.9, \dots, 149.9, 150s]$$

As all bursts for a given model now share a common domain, an average light curve can be calculated by point-wise averaging of the luminosity points. Once the average light curve is created, the script records the peak luminosity of the average light curve and calculates its integrated luminosity by the following equation:

$$\int_{-10}^{150} L(t)dt \quad (1.5)$$

The metric used to compare the models to the baseline, which will now be referred to as integrated luminosity difference, was defined by Cyburt *et al.* [Cyb16] as

$$M_{LC}^{(i)} = \int_{-10}^{150} |\langle L_i(t) \rangle - \langle L_0(t) \rangle| dt \quad (1.6)$$

Here,  $LC$  refers to the time the light curve is plotted over, which in our study is  $-10 < t_{peak} = 0 < 150$ ,  $\langle L_i(t) \rangle$  refers to the average light curve of modified model  $i$  and  $\langle L_0(t) \rangle$  refers to the average light curve of the baseline model.

The integrated luminosity difference is then scaled by the baseline to give the relative difference as a ratio of the baseline integrated luminosity. These values are also compared with real light curves from observation, see Fig. 1.15.

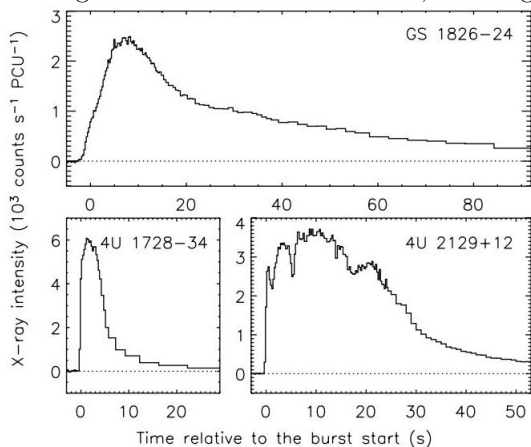


**Figure 1.15:** Example observational light curves from Galloway *et al.* [Gal08] of GS-1826-24, collected by the Rossi X-ray Timing Explorer.

Integrated energy will be calculated by the same python script used to calculate integrated luminosity. The only change necessary is denoting the energy data, which is simply a different column in the data set. The resulting calculations (Eqns. 1.5 and 1.6) follow accordingly, with  $E(t)$  replacing  $L(t)$ .

Part I of the study is nearly complete as the burst period, benchmark points, and integrated luminosity of the models have been analyzed. Below Table 1.2 displays a few reactions with a considerable effect on integrated luminosity. At this time, the models are being re-run to print the abundance profiles. Once the analysis is complete, the models with the largest change from baseline will move on to the fine-resolution Part II.

In Part II, the analysis will be repeated with the rates varied within their actual recorded uncertainties. Finally all the information gleaned from this work will be compared with real-world values. This information will be used to prioritize future experimental work at various universities and national labs, especially at the upcoming Facility for Rare Isotope Beams, set to come online very soon [Bal14].

**Table 1.2:** Integrated Luminosity Difference (Part I), Select Reactions

Reaction	Upper/Lower Limit	$M_{LC}$ (scaled)
$^{54}\text{Co} (n, \gamma) ^{55}\text{Co}$	Upper	0.422
$^7\text{L} (p, \alpha) ^4\text{He}$	Lower	0.221
$^{27}\text{Si} (p, \gamma) ^{28}\text{P}$	Lower	0.220
$^{34}\text{Ar} (n, \gamma) ^{35}\text{Ar}$	Upper	0.212
$^{31}\text{Ar} (n, \gamma) ^{32}\text{Ar}$	Upper	0.209

[Bal14] A. B. Balantekin *et al.*, Mod. Phys. Lett. A, **29**, 1430010 (2014).

[Cyb16] R. H. Cyburt *et al.*, Astrophys. J., **830**, 55 (2016).

[Fie16] C. E. Fields *et al.*, Astrophys. J., **823**, 46 (2016).

[Gal08] D. K. Galloway *et al.*, Astrophys. J. Suppl., **179**, 360 (2008).

[Ili08] C. Iliadis, *Nuclear Physics of Stars*, Wiley, 2008.

[In'11] J. J. In't Zand, (2011), arXiv:1102.3345 [astro-ph.HE].

[Sch06] H. Schatz and K. E. Rehm, Nucl. Phys. A, **777**, 601 (2006).

## 1.5 Data Evaluation of ${}^9\text{C}$

B. GREES, *Lipscomb University, Nashville, TN*; J.H. KELLEY, *TUNL*

TUNL is part of an international group of Nuclear Structure and Decay Data evaluators (NSDD) that perform nuclear structure and decay data evaluations for the Evaluated Nuclear Structure Data File (ENSDF). In addition, any recently published experimental nuclear data are compiled for the Experimental Unevaluated Nuclear Data List (XUNDL). ENSDF contains recommended data on nuclear properties and parameters and thus this data is important for various nuclear applications. All published data on  ${}^9\text{C}$  was reviewed and evaluated. The current  ${}^9\text{C}$  ENSDF was updated and prepared to submit, and a new dataset of recommended properties, such as decay modes, level energies, and radiation properties was produced.

As a member of the NSDD and the USNDP (U.S. Nuclear Data Program), TUNL works on performing compilations and evaluations for the ENSDF and XUNDL databases. The primary difference between these two databases is how much and what data they comprise. XUNDL is a compilation of just one recently published article and includes a brief overview of the primary data observed in the article. ENSDF, however, is much more comprehensive in that it is a complete evaluation of all experimental nuclear data pertaining to a certain nuclide.

In addition, ENSDF contains a recommended and adopted dataset of nuclear properties and parameters for that particular nuclide. These nuclear properties and parameters include decay modes, level energies and lifetimes, and radiation properties. Thus, this data is essential for a vast range of nuclear applications including, but not limited to, planning and interpreting basic scientific experiments, nuclear medicine, reactor design and operation, radiation safety, environmental science, geophysics, and materials science.

At TUNL, the group's activities are to assess literature and identify any relevant publications in the mass region from  $A=3$  to 20 and then compile them into the XUNDL database and to perform evaluations of the compiled literature for ENSDF.

The majority of our work over the course of the program was primarily working on updating the  ${}^9\text{C}$  ENSDF. As discussed earlier, the  ${}^9\text{C}$  ENSDF is a complete evaluation of all experimental data on  ${}^9\text{C}$  ranging from its initial discovery to any recently published data. Thus, we evaluated all publications on

${}^9\text{C}$  and assessed their contributions to the  ${}^9\text{C}$  ENSDF and to a new adopted dataset.

The first experimentally determined occurrence of  ${}^9\text{C}$  was found in 1956 [Swa56] during a survey of nuclear photographic emulsion (see Fig. 1.16). Nuclear photographic emulsion is a method of detecting short-lived radioisotopes. The way this method works is by tracking the path of the decay fragments of the isotope through the emulsion and producing a photograph of it.

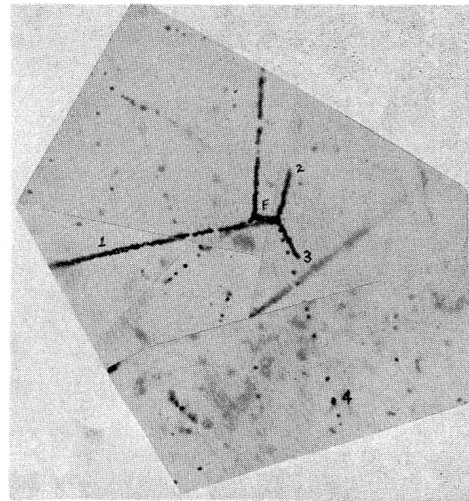


FIG. 1. A photograph of an event interpreted as the beta decay of  ${}^9\text{C}$ . The  ${}^9\text{C}$  nucleus (track  $F$ ) was produced in star ( $A$ ) and disintegrated into a proton, two alpha particles, and a positron (tracks 1, 2, 3, and 4, respectively).

Figure 1.16: Photographic Emulsion of  ${}^9\text{C}$

In 1956, it was found that after striking a photo-

graphic plate with 3 GeV protons, a particular decay pattern was observed. The decay fragments were 2 alpha particles, a beta particle, and 1 proton. The possible isotopes for this were either  ${}^9\text{C}$  or  ${}^9\text{Be}$ . However,  ${}^9\text{Be}$  is a stable isotope so it was determined that this was the first occurrence of  ${}^9\text{C}$ .

There have been four half-life measurements of  ${}^9\text{C}$  since its first observed occurrence. These four measurements produce an average recommended value of 126.5 (1) ms. The earliest measurement was in 1965 [Har65] and used  ${}^{12}\text{C}(p,d2n){}^9\text{C}$ ,  ${}^{10}\text{B}(p,2n){}^9\text{C}$ , and  ${}^{11}\text{B}(p,3n){}^9\text{C}$  reactions to produce  ${}^9\text{C}$  and yielded a half-life of 127.0 (3) ms. In this experiment, the first  ${}^9\text{C}$  decay scheme was produced (see Fig. 1.17). This is especially noteworthy because it shows that  ${}^9\text{C}$  is a delayed proton precursor isotope.

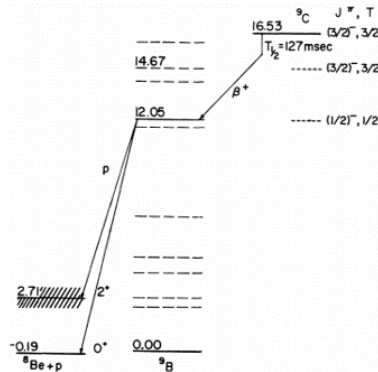


Figure 1.17: First  ${}^9\text{C}$  Decay Scheme

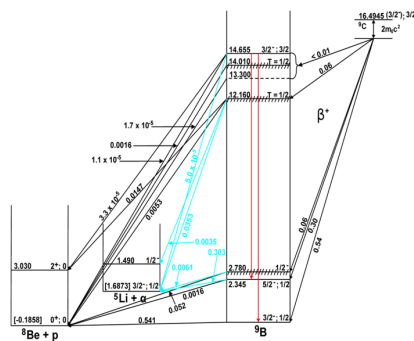


Figure 1.18: Current  ${}^9\text{C}$  Decay Scheme

That  ${}^9\text{C}$  is a delayed proton precursor means that it itself is beta unstable and beta decays to  ${}^9\text{B}$ . However,  ${}^9\text{B}$  is also very proton-unstable and very quickly proton decays to  ${}^8\text{Be}$  hence the term "delayed proton".

This is also what was observed in the nuclear photographic emulsion in Fig. 1.16. In that experiment,

the 3 GeV protons come in and bombard the photographic plate to produce  ${}^9\text{C}$ . The  ${}^9\text{C}$  travels a little bit before beta decaying into  ${}^9\text{B}$ . The  ${}^9\text{B}$  is very proton unstable and so it decays by shooting off a proton in one direction and the  ${}^8\text{Be}$  recoils in the other direction before it decays into 2 alpha particles. Fig. 1.18 shows the current  ${}^9\text{C}$  decay scheme.

The current observed level states of  ${}^9\text{C}$  can be found below in Table 1.3. The ground state has a  $3/2^-$  spin parity. The first excited state is the  $1/2^-$  state at 2.218 MeV and was measured in 1974 [Ben74] using a  ${}^{12}\text{C}({}^3\text{He}, {}^6\text{He}){}^9\text{C}$  reaction. The  $5/2^-$  state was measured in 2007 [Rog07] and  $5/2^+$  state was measured in 2019 [Hoo19]. Both were measured using resonant elastic scattering of protons on  ${}^8\text{B}$ . In both measurements a R-matrix analysis was applied to produce a fit to the data. The 9 and 15 MeV levels were found in a doubly coherent pion production experiment in 1984.

Table 1.3: Level States of  ${}^9\text{C}$

Energy (keV)	$J^\pi$	Width
Ground State	$3/2^-$	0
2218(11)	$1/2^-$	52(11)
3549(20)	$5/2^-$	672(50)
4300(300)	$5/2^+$	4.0 MeV +2.0 -1.4
6400?	$7/2^-$	1100
9 MeV		Broad
15 MeV		Broad

The  $7/2^-$  state is interesting because while it wasn't directly measured in any experiment as of today, its inclusion in the R-matrix analysis in the 2019 experiment produced a much better fit to the observed data. However, that experiment extended up to 6.3 MeV and the probable  $7/2^-$  state was placed at around 6.4 MeV. Thus, this state is subject to future experimental confirmation.

[Ben74] W. Benenson and E. Kashy, Phys. Rev. C, **10**, 2633 (1974).

[Har65] J. C. Hardy *et al.*, Phys. Rev. Lett., **14**, 376 (1965).

[Hoo19] J. Hooker *et al.*, Phys. Rev., **100**, 054618 (2019).

[Rog07] G. Rogachev *et al.*, Phys. Rev. C, **75**, 014603 (2007).

[Swa56] M. S. Swami, J. Schneps, and W. F. Fry, Phys. Rev., **103**, 1134 (1956).

## 1.6 Analysis of Activation Data for Short-Lived Radioisotopes using the RABITTS Transfer System

O. DICKINSON, *Providence College, Providence, RI*; KRISHICHAYAN, *TUNL*

Basic nuclear reaction cross-section data, such as  $(n, 2n)$ ,  $(n, \gamma)$  and  $(\gamma, n)$ , from the production of short-lived isotopes are critically important to a breadth of scientific fields including applications relevant to national security, medical isotopes, and fission and fusion reactor technology. However, little experimental data are available due to various limitations with one primary factor being poor counting statistics. This limitation can be overcome by using the cyclic activation technique by way of a fast-irradiated sample transfer system. With the availability of a fast transfer system, namely, RABITTS at TUNL, the cyclic activation technique can be used to study reaction cross sections for nuclei having half-lives between seconds and minutes. The primary isotopes of interest are  $^{73}\text{Ge}$ ,  $^{77}\text{Ge}$ ,  $^{91}\text{Mo}$ ,  $^{114}\text{In}$ , and  $^{116}\text{In}$ , which will be produced using quasi-monoenergetic neutron beams from the 10 MV tandem accelerator at TUNL. An array of highly efficient and broad energy germanium detectors will be used for the gamma-ray counting. A detailed energy and efficiency calibration of the detector array along with the conceptual and computation work related to the project will be presented in this report.

Precise neutron-induced reaction cross-section measurements are very useful information for basic nuclear physics as well applications relevant to national security, medical isotopes, and fission and fusion reactor technology. Neutron activation analysis can be used to remotely detect the chemical composition of materials. This is because different elements release characteristic radiation when they absorb neutrons. This makes it useful in many fields related to mineral exploration and security.

Most experimental cross-section data exists for reactions leading to relatively long-lived nuclei ( $\text{min} \leq T_{1/2} \leq \text{hr}$ ) and most of these measurements are single average neutron energy measurements. However, in the case of the reactions leading to relatively short-lived product nuclei the experimental data are either discrepant or very scarce (due to various associated limitations including poor counting statistics, low neutron flux etc.). One of the solutions available for this situation is to apply the cyclic activation method utilizing a fast irradiated sample transfer system, which allows cyclic activation and counting with predetermined time intervals.

During this project, a literature survey (using EXFOR) was conducted on the isotopes of interest. Previous experimental setups using accelerators by the method of neutron capture with similar detector setups as used in the Tandem laboratory were stud-

ied. The reactions of interest were those with incident neutron beam energies from 0.5 to 14.8 MeV. Looking at the cross-section data of these potential isotopes of interest, there were five that had little to no data:  $^{73}\text{Ge}$ ,  $^{77}\text{Ge}$ ,  $^{91}\text{Mo}$ ,  $^{114}\text{In}$ , and  $^{116}\text{In}$ .

The difficulty in measuring the reaction cross sections of short lived nuclei has been solved at TUNL by RABITTS — **R**apid **B**elt **D**riven **I**rradiated **T**arget **T**ransfer **S**ystem. RABITTS allows for the possibility of transferring short-lived isotope samples to a nearby counting room with limited background radiation.

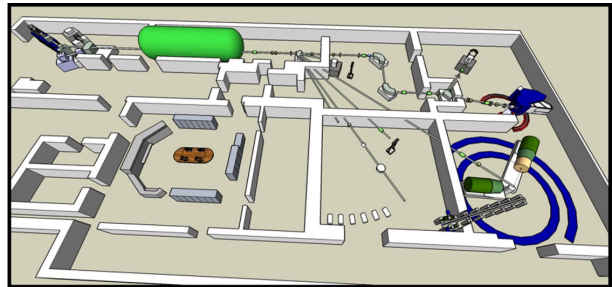
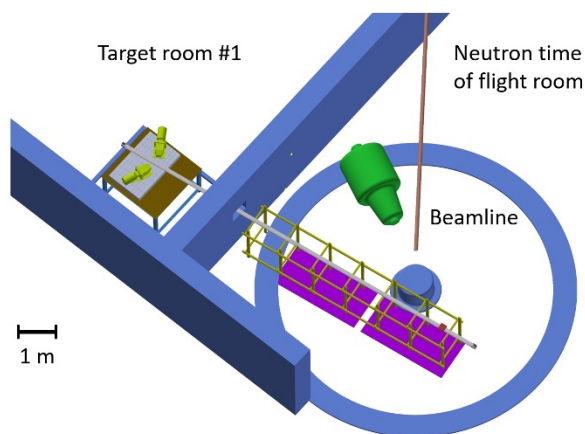
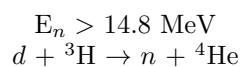
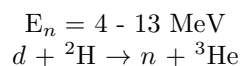
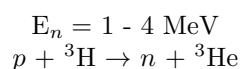


Figure 1.19: Tandem Lab floorplan

Figure 1.19 shows a view of the Tandem Accelerator Laboratory where the 10 meter RABITTS track is used. RABITTS allows for cyclic neutron activation analysis. The 10 meter transfer system has

been developed with transit times as lows as 1.0 second. These systems are used in the Tandem Accelerator Laboratory along with monoenergetic neutron beams. The 10 MV Van de Graaff accelerator is the large green cylindrical object located in the top left corner of the figure. Quasi-monoenergetic neutron beams are produced at TUNL through three different reactions depending on the incident neutron energies needed for isotope production in nuclear capture reactions. These monoenergetic neutron beams range from 0.5 to 14.8 MeV.



**Figure 1.20: Neutron Time of Flight Room Featuring RABITTS**

Figure 1.20 shows a schematic of the 10 m RABITTS. The target is irradiated in the center of a large 10 m x 10 m room. Once irradiated the sample is then transported through a thick concrete wall to a low background counting area via RABITTS. In target room #1, two HPGe detectors are used and positioned 90 degrees to the target plane.

The data specifically needed for spectrometer calibration are the gamma-ray energies, the half-lives,

and the accurate activity of the isotopes at the time of irradiation.

Reference Date: 01-February-2018 12:00 PM EST

TCC Mixture

Isotope	Gamma-Ray Energy, keV	Half-Life, d	Activity, Bq	Flux, s <sup>-1</sup>	Uncertainty			Calibration Method**
					u <sub>e</sub> , %	u <sub>p</sub> , %	u <sub>r</sub> , %	
Am-241	59.5	1.580E+05	6.625E+03	2.378E+03	0.1	1.8	3.6	ISC
Cd-109	83.9	4.614E+02	5.955E+04	2.204E+03	0.1	2.3	4.6	IC
Co-57	122.1	2.717E+02	1.527E+03	1.307E+03	0.1	1.7	3.5	IC
Ce-139	165.9	1.376E+02	2.095E+03	1.676E+03	0.1	1.8	3.6	IC
Hg-203	279.2	4.659E+01	4.940E+03	4.029E+03	0.1	1.7	3.5	IC
Sn-113	391.7	1.151E+02	3.334E+03	2.166E+03	0.1	1.7	3.5	IC
Cs-134	604.7	7.543E+02	7.742E+03	7.559E+03	0.1	1.7	3.5	IC
Cs-134	795.9	—	—	6.617E+03	0.1	1.7	3.5	—
Cs-137	661.7	1.099E+04	1.760E+03	1.497E+03	0.1	1.7	3.5	IC
Mn-54	834.8	3.121E+02	4.193E+03	4.193E+03	0.1	1.7	3.3	IC
Y-88	898.0	1.066E+02	7.659E+03	7.176E+03	0.1	1.7	3.3	IC
Y-89	1836.1	—	—	7.597E+03	0.1	1.7	3.3	—
Zn-65	1115.5	2.439E+02	1.107E+04	5.540E+03	0.1	1.7	3.5	IC

\*Uncertainty: U - Relative expanded uncertainty, k = 2. See NIST Technical Note 1287, "Guidelines for Evaluating and Expressing the Uncertainty of NIST Measurement Results." \*\*Calibration Methods: 4n LS - 4n Liquid Scintillation Counting, HPGe - High Purity Germanium Gamma-Ray Spectrometer, IC - Ionization Chamber.

**Figure 1.21: Spectrometer Calibration Data**

The object of energy calibration is to derive a relationship between the peak position in the spectrum and the corresponding gamma-ray energy. It is important the calibration energies cover the entire range for which the spectrometer will be used. The computer measures the peak position relative to the channel number and finds the energy/channel relationship. The reported efficiency of a HPGe detector is a relative efficiency which compares the detection of the <sup>60</sup>Co gamma ray at 1332 keV of the detector to that of a sodium iodide scintillation detector.

Most of this summer work was spent understanding how the HPGe scintillation detectors operate, the processes of different nuclear reactions and decay modes, and learning about TUNL and the RABITTS system. Through the work it was possible to obtain a dataset of isotopes which have limited cross-section data with an experimental setup such as the one in TUNL. The next steps would be to obtain samples of these isotopes of interest, properly setup energy calibrations of the detectors, and irradiate the samples to acquire experimental cross-section data.

[Bha14] C. Bhatia *et al.*, Nucl. Instrum. Methods, **757**, 7 (2014).

[Gil08] G. R. Gilmore, *Practical Gamma-ray Spectroscopy*, John Wiley & Sons, Inc., 2nd edition, 2008.

[Gre11] R. Greenberg, P. Bode, and E. Fernandes, Spectrochim. Acta B, **66**, 193 (2011).

[Lon20] R. Longland, 2020.

# Research Based at CERN

---

Chapter 2

## 2.1 Exploring Track Trigger Parameters for SUEPs

J. NELSON, *Westminster College, New Wilmington, PA*; K. PACHAL, *Duke University, Durham, NC*

CERN’s ATLAS and CMS experiments were designed with prompt and standard model particles in mind. New desired searches, primarily for long lived particles (LLPs) and exotic signatures, demand new considerations in the design and implementation of hardware level track triggering algorithms. This study simulates such events so as to find the collection of triggering parameters that best suit a wide range of LLP and exotic signatures. One such signature is SUEPs, or stable unclustered energy patterns. We have found that for this signature, low parent masses and high transverse momentum thresholds lower efficiency substantially, while the number of tracks per event threshold is robust. Additional efficiency testing must be conducted for displaced leptons, displaced vertices, and stable charged particles before appropriate parameters can be identified.

The sheer volume of data produced by CERN’s ATLAS and CMS experiments is too great to permanently store for later analysis. Given only a portion of the data produced contains events of interest, a need exists to distinguish between promising and less promising events. Algorithms analyze certain aspects of events as they occur to determine if the event meets conditions necessary to warrant storing the data for further analysis.

Currently, detectors yield low efficiencies for appropriately triggering on Beyond Standard Model (BSM) events [Lee19]. Additionally, triggering is often performed on a software level, post-event, leading to data storage concerns. To better search for LLPs and other exotic signatures, new triggers must be developed at a hardware level to both alleviate storage concerns and account for their unique properties, predominantly particle tracks [Kna17].

This study intends to determine the set of parameters best suited for the collection of LLP and exotic signatures. To date, only SUEPs have been tested. In addition, super-symmetric and exotic higgs models will be considered, covering SUEPs, displaced leptons, displaced vertices, and stable charged particle signatures [Pet20].

SUEP events are created (see Fig. 2.1) via a strongly coupled hidden valley accessed by a scalar moderator, in this case a standard model higgs boson. The higgs then decays into a spherically symmetric shower of dark mesons. These dark mesons interact with dark photons and further decay into pairs of

standard model particles. SUEPs, while easier to analyze given their prompt decays, produce a jumble of tracks with low transverse momentum ( $p_T$ ), momentum only in the transverse plane, making it somewhat difficult to differentiate from background.

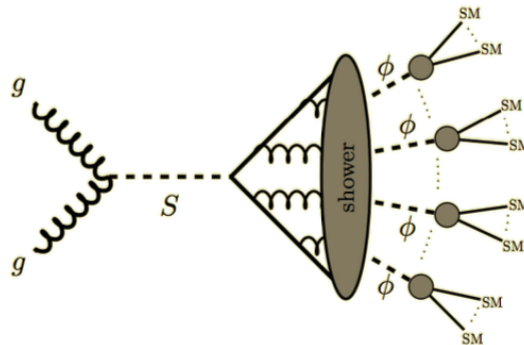


Figure 2.1: SUEP Model

10,000 event simulations were created for each of six parent higgs masses (125, 200, 400, 600, 800, and 1,000 GeV). For each of these simulated events, daughter particles of the standard model higgs were first checked to ensure they would be “seen” by the detectors. For an event to be seen, all daughter particles must be charged, stable, and within the angular coverage of the ATLAS tracker.

Provided these conditions are met, the event is then passed through a series of checks. If all daughter particles have a  $p_T$  greater than the threshold and

the event has more particle tracks than the threshold, the event passes for that particular track count and  $p_T$  combination. There are three  $p_T$  thresholds: 0.5, 1, and 2 GeV, and three track count thresholds: 100, 150, and 200, making for nine combinations. These checks help to ensure they can be separated from background via triggering.

For each parent mass, all 10,000 SUEP events were tested as stated above. Efficiencies for each of the possible  $p_T$  and number of particle track combinations were then calculated by the simple ratio of events that passed both checks for that combination to the total event count. Errors were propagated via the binomial method.

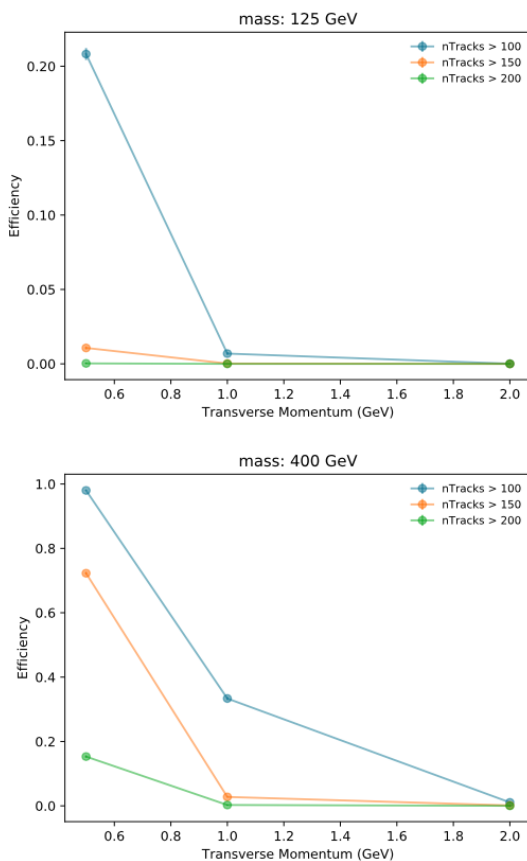


Figure 2.2: Fixed Mass Efficiencies

Efficiencies were plotted for visualization, with one property held fixed, another varied along the x-axis, and the third displayed as separate lines on the plot. From these plots, three overall trends are apparent. First, as parent masses increase, so too do efficiencies. Most significantly are the extreme lows for the 125 and 200 GeV parent masses. By 400 GeV, we

see efficiencies rise towards reasonable levels. Fig. 2.2 shows the fixed mass efficiency vs.  $p_T$  plots for 125 and 400 GeV.

The next notable trend is the near-zero efficiency for all  $p_T > 2$  GeV cases. As seen in Fig. 2.3, less than 10% of seen events meet any combination of required track count and  $p_T > 2$  GeV. Cutting the threshold down to 1 GeV greatly increases efficiencies. Lastly, signals are quite robust to track count selection (Fig. 2.4).

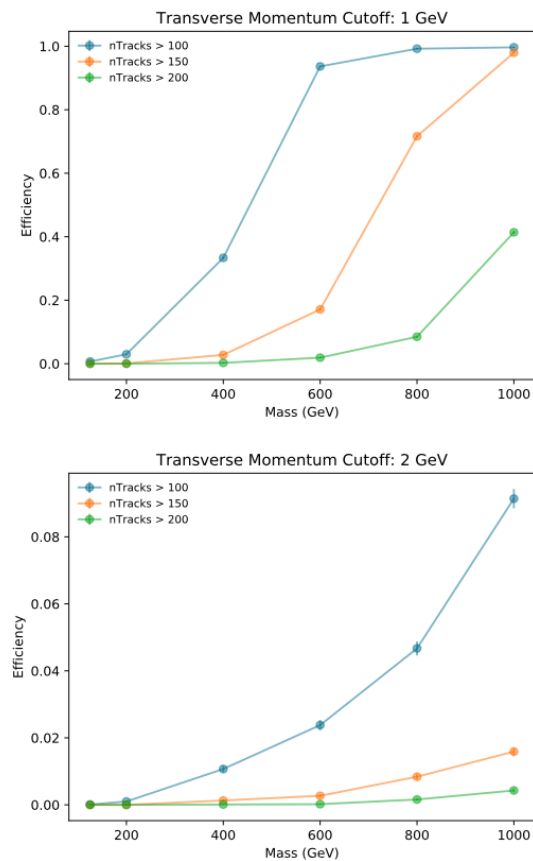


Figure 2.3: Fixed Transverse Momentum Efficiencies

Given the poor efficiencies with high  $p_T$  requirements, triggers would need to rely less on restricting  $p_T$ , and more on parameter features such as high track counts. While this should be manageable for ATLAS, CMS's more restrictive  $p_T$  thresholds make this more difficult.

One possible alternative parameter is HT, which is a measure of the scalar sum of  $p_T$  for all event tracks. As seen in Fig. 2.5, with the current CMS threshold for required HT of roughly 450 GeV, using

this parameter would allow a sufficient percentage of events to pass, yielding reasonable efficiencies.

We find both low parent masses and high  $p_T$  thresholds lead to low trigger efficiencies, predominantly with high  $p_T$ , while the track count selections are robust. From this we conclude that triggering on SUEPs would benefit from high track count requirements and less restrictive  $p_T$  requirements, while a HT-based trigger appears promising for CMS application.

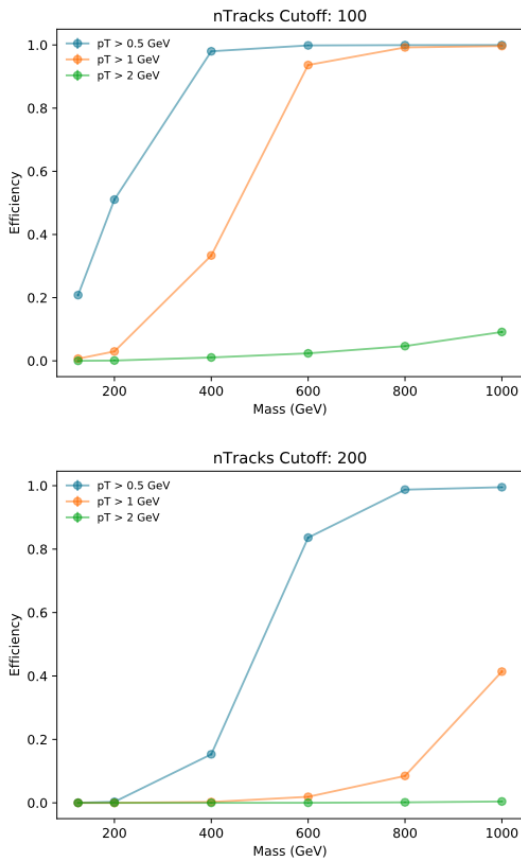


Figure 2.4: Fixed Tracks Efficiencies

Future work will focus on completing the same analysis for displaced leptons, displaced vertices, and stable charged particles. Efficiencies will be compared to determine the best set of parameters for all

models. Lastly, background rates will be estimated for trigger selections.

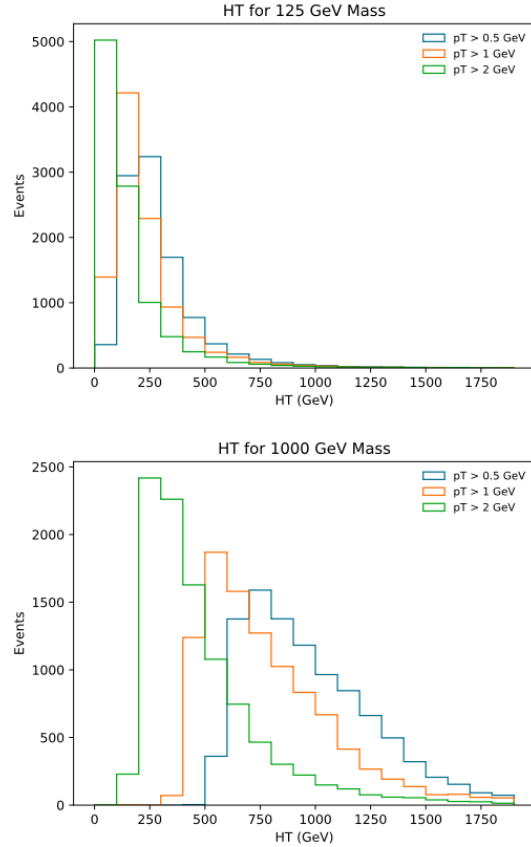


Figure 2.5: HT

[Kna17] S. Knapen *et al.*, J. High Energy Phys., **8** (2017).

[Lee19] L. Lee *et al.*, Prog. Part. Nucl. Phys., **106**, 210 (2019).

[Pet20] K. D. Petrillo, T. Holmes, and K. Pachal, *Track-based Triggers for Exotic Signatures*, 2020, <https://www.snowmass21.org/docs/files/summaries/EF/SNOWMASS21-EF9-IF4-008.pdf>.

## 2.2 Using Machine Learning to Improve the Sensitivity of $t\bar{t}$ Resonance Searches

A. PARTENHEIMER, *Truman State University, Kirksville, MO*; M. KRUSE, *Duke University, Durham, NC*

Proton-proton collisions resulting in four top quarks may be relevant for probing Beyond-Standard-Model physics, and are being studied by the ATLAS experiment on the Large Hadron Collider. While four-tops final states are predicted by the Standard Model, they are rare, and therefore difficult to detect. Even though the ATLAS experiment has evidence of the four-tops final state, it still has not achieved the  $5\sigma$  certainty required to claim observation. Furthermore, in order to distinguish production of a Beyond-Standard-Model  $t\bar{t}$  heavy resonance the current analysis would require better resolution of the four-tops final state. This project examined the feasibility of using machine learning with TensorFlow to improve sensitivity in  $t\bar{t}$  resonance searches.

The Four-Tops project on the ATLAS experiment searches for proton-proton collisions that result in four top quarks, as this may be linked to Beyond-Standard-Model (BSM) physics. While machine learning (ML) is often used to separate signal from background in detector experiments, applying ML analysis to the Four-Tops project would require a different approach. Here, a ML framework would be required to determine probabilities that two decay products came from the same source. This "sorting" of decay products could be more taxing on the neural network, and may not be feasible given the large amount of data it would be required to handle.

The top quark is the heaviest elementary particle in the Standard Model, and is predicted to couple to BSM resonances [Aab19]. Because of this prediction, proton-proton collisions resulting in four top quarks are of particular interest. Four-tops final states are predicted by the Standard Model, but are rare and therefore difficult to detect. The ATLAS experiment has evidence for the four-tops final state, but not to the  $5\sigma$  certainty required in to claim observation. A better resolution of the four-tops final state could show the presence of four-tops production mediated by a BSM resonance. An example diagram of four-tops production via a BSM resonance is shown in Fig. 2.6.

In order to determine the mass of a BSM heavy resonance created during four-tops production, the analysis would need to be able to distinguish between resonance and spectator decay products. While the resonance and spectator decay products are intrinsi-

cally identical, they have distinct kinematics.

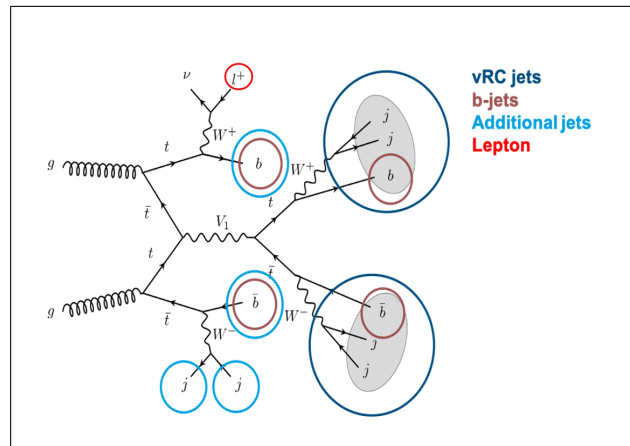


**Figure 2.6:** Theoretical production of four-tops via a BSM heavy resonance. Two gluons interact by the strong force, producing top-antitop pairs. Two top quarks form a BSM heavy resonance ( $V_1$ ) while the other two become spectators. The heavy resonance decays back into a top-antitop pair, which then decay to W-bosons and bottom quarks.

As the BSM heavy resonance is assumed to have a large mass, it imparts a high energy to its top quark decay products. Therefore, the resonance top quarks are more highly relativistic than the spectator top quarks. The relativistic effect on the resonance top quarks is such that the resonance top quarks appear to be more closely spaced, or collimated, than the

spectators.

There are two other properties that distinguish decay products of resonance vs. spectator top quarks. Because the resonance tops have a higher momentum than their spectator counterparts, the b-jets they produce can generally have a higher transverse momentum (see top plots in Fig. 2.7). In addition, while maximum  $\Delta R$  ( $\Delta R = \sqrt{\Delta\phi^2 + \Delta\eta^2}$ , where  $\phi$  is the azimuthal angle and  $\eta$  is the pseudorapidity) for the spectator decay products often has values as large as  $\Delta R = \pi$ , corresponding to a  $180^\circ$  spread between the decay products, the more-collimated resonance decay products usually have a  $\Delta R = \frac{\pi}{4}$ . This property is illustrated in the bottom plots in Fig. 2.7.

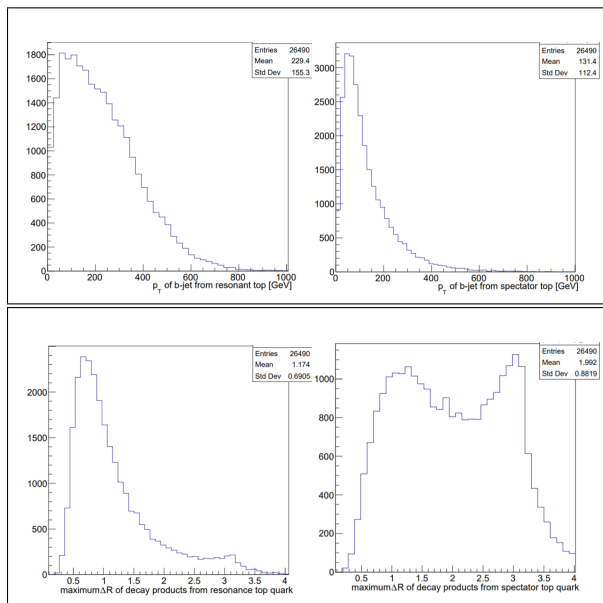


**Figure 2.7:** Comparison of event kinematics for resonance (left) vs. spectator (right) decay products. The top plots show the transverse momentum of the b-jets produced in four-tops decay. The bottom plots illustrate the difference in  $\Delta R$  between resonance and spectator top quark decay products.

The current analysis is attempting to distinguish between resonance and spectator decay products by defining "reclustered jets": a highly-collimated group of two jets and a b-jet. While this analysis is still being developed, there are indications that it may be sub-optimal, which motivates the use of a ML approach.

We are training our neural network with TensorFlow, a Python-based tensor manipulation frame-

work [Cho18]. To test the feasibility of using the neural network in Four-Tops analysis, we are first training the neural network on simulated  $t\bar{t}$  samples only. If the neural network is able to successfully analyze  $t\bar{t}$  pairs, it may be feasible to extend its application to four-tops events.

Because  $t\bar{t}$  decay products can only be distinguished by their kinematics, the neural network is given particles' four-vectors:  $\langle p_x, p_y, p_z, E \rangle$ . The particles are grouped into events corresponding to individual  $t\bar{t}$  pairs. The neural network should be able to use the four-vector information to deduce other distinguishing quantities such as  $\Delta R$  or the transverse momentum  $p_T$ , as these quantities can be calculated directly from the four-vectors.

Rather than considering properties of individual particles, in this analysis the neural network would be required to compare all particles within an event. We considered two approaches by which the neural network should compare particles, and determined qualitatively that the latter of the two is better, though the other approach is still worth examining.

1. In the first approach, the neural network is given every possible arrangement of decay products into groups of three, and must then determine which arrangement most likely corresponds to the sets produced by the parent top quarks.
2. In the second approach, one particle is separated from each event to be used as a point of comparison. For each subsequent particle in that event, the neural network is given the particle's four-vector, as well as the four-vector from the particle that was removed for comparison. The neural network should then return a probability that the two particles originated from the same parent. Ideally, the neural network would return a set of two high and three low probabilities per event.

We determined that the second approach is the more promising of the two: the order in which the neural network is fed information is more straightforward than in the first, so the neural network is less likely to become overwhelmed. In addition, the neural network's performance is less likely to be affected by a particle lost in the detector, as the missing particle can simply be omitted from the comparison. Finally, the particle extracted for comparison can be strategically selected: for example, the highest- $p_T$  particle would be most clearly observed by the detector, and would therefore make a good point of comparison for other particles.

The current Four-Tops analysis is seeking to distinguish decay products by defining "reclustered jets", but there is evidence that this approach may be sub-optimal. A machine learning approach to the four-tops analysis is being developed. This approach uses TensorFlow to train a neural network to distinguish between resonance and spectator decay products based on their kinematics. In an initial approach, a neural network is being trained to analyze decay products coming from simulated  $t\bar{t}$  samples. If

the neural network is able to handle an analysis of  $t\bar{t}$  samples only, it may be feasible to implement a similar approach on the Four-Tops analysis.

---

[Aab19] M. Aaboud *et al.*, Phys. Rev. D, **99**, 052009 (2019).

[Cho18] F. Chollet, *Deep Learning with Python*, Manning Publications Co., 2018.

# Index

Dickinson, O., 15

Grees, B., 13

Lapinski, I., 10

Nelson, J., 18

Partenheimer, A., 21

Rosado Del Rio, L., 4

Strickland, B., 7

Sturm, M., 2